A stochastic view of the 2020 Elazığ Mw 6.8 earthquake

Théa Ragon[1], Mark Simons[2], Quentin Bletery[3], Olivier Cavalié[3], and Eric J. Fielding[4]

[1]California Institute of Technology
[2]Caltech
[3]Université Côte d'Azur, IRD, CNRS, Observatoire de la Côte d'Azur, Geoazur
[4]Jet Propulsion Laboratory, Caltech

November 24, 2022

Abstract

Until the Mw 6.8 Elazığ earthquake ruptured the central portion of the East Anatolian Fault (EAF) on January 24, 2020, the region had only experienced moderate magnitude (Mw 6.2) earthquakes over the last century. Here, we use geodetic data to constrain a model of subsurface fault slip. We adopt an unregularized Bayesian sampling approach relying solely on physically justifiable prior information and account for uncertainties in both the assumed elastic structure and fault geometry. The rupture of the Elazığ earthquake was bilateral, with two primary disconnected regions of slip. This rupture pattern may be controlled by structural complexity. Both the Elazığ and 2010 Mw 6.1 Kovancılar events ruptured portions of the central EAF that are believed to be coupled during interseismic periods, and the Palu segment is the last portion of the EAF showing a large deficit of fault slip which has not yet ruptured in the last 145 years.

A stochastic view of the 2020 Elazığ M_w6.8 earthquake

Théa Ragon[1], Mark Simons[1], Quentin Bletery[2], Olivier Cavalié[2], Eric Fielding[3]

[1]Seismological Laboratory, California Institute of Technology, Pasadena, CA, USA.
[2]Université Côte dAzur, IRD, CNRS, Observatoire de la Côte dAzur, Géoazur, France.
[3]Jet Propulsion Laboratory, California Institute of Technology, Pasadena, CA, USA.

Key Points:

- We infer a stochastic model for the distribution of subsurface fault slip associated with the 2020 Elazığ earthquake
- We account for uncertainties in both the depth-dependence of the assumed elastic structure and the location and geometry of the fault
- Our models are characterized by two primary patches of fault slip where distribution appears to be controlled by geometrical complexities

Corresponding author: Théa Ragon, `tragon@caltech.edu`

Abstract

Until the M_w 6.8 Elazığ earthquake ruptured the central portion of the East Anatolian Fault (EAF) on January 24, 2020, the region had only experienced moderate magnitude ($M_w < 6.2$) earthquakes over the last century. Here, we use geodetic data to constrain a model of subsurface fault slip. We adopt an unregularized Bayesian sampling approach relying solely on physically justifiable prior information and account for uncertainties in both the assumed elastic structure and fault geometry. The rupture of the Elazığ earthquake was bilateral, with two primary disconnected regions of slip. This rupture pattern may be controlled by structural complexity. Both the Elazığ and 2010 M_w 6.1 Kovancılar events ruptured portions of the central EAF that are believed to be coupled during interseismic periods, and the Palu segment is the last portion of the EAF showing a large deficit of fault slip which has not yet ruptured in the last 145 years.

Plain Language Summary

The Elazığ earthquake ruptured the central portion of the East Anatolian Fault (EAF), a major strike-slip fault in eastern Turkey, on January 24, 2020. Before this event, the region had only experienced moderate magnitude earthquakes over the last century. We aim at understanding the rupture of this earthquake, and how it relates to the historical ruptures of the EAF. To do so, we use geodetic observations of the deformation at the surface to image the subsurface slip on the fault that occurred during the earthquake. As the characteristics of the crust are poorly known, we make realistic assumptions on the fault geometry and Earth structure, and build on novel approaches to account for the possible biases of our assumptions and to characterize the uncertainties of the imaged slip. We suggest that the Elazığ earthquake rupture may be controlled by structural complexity of the fault, and that two main regions of slip surround the fault bend responsible for the nucleation of the rupture. We also suggest that the fault segment located between Lake Hazar and the city of Palu is the last portion of the central EAF, showing a large deficit of the fault slip, which has not yet ruptured in the last 145 years.

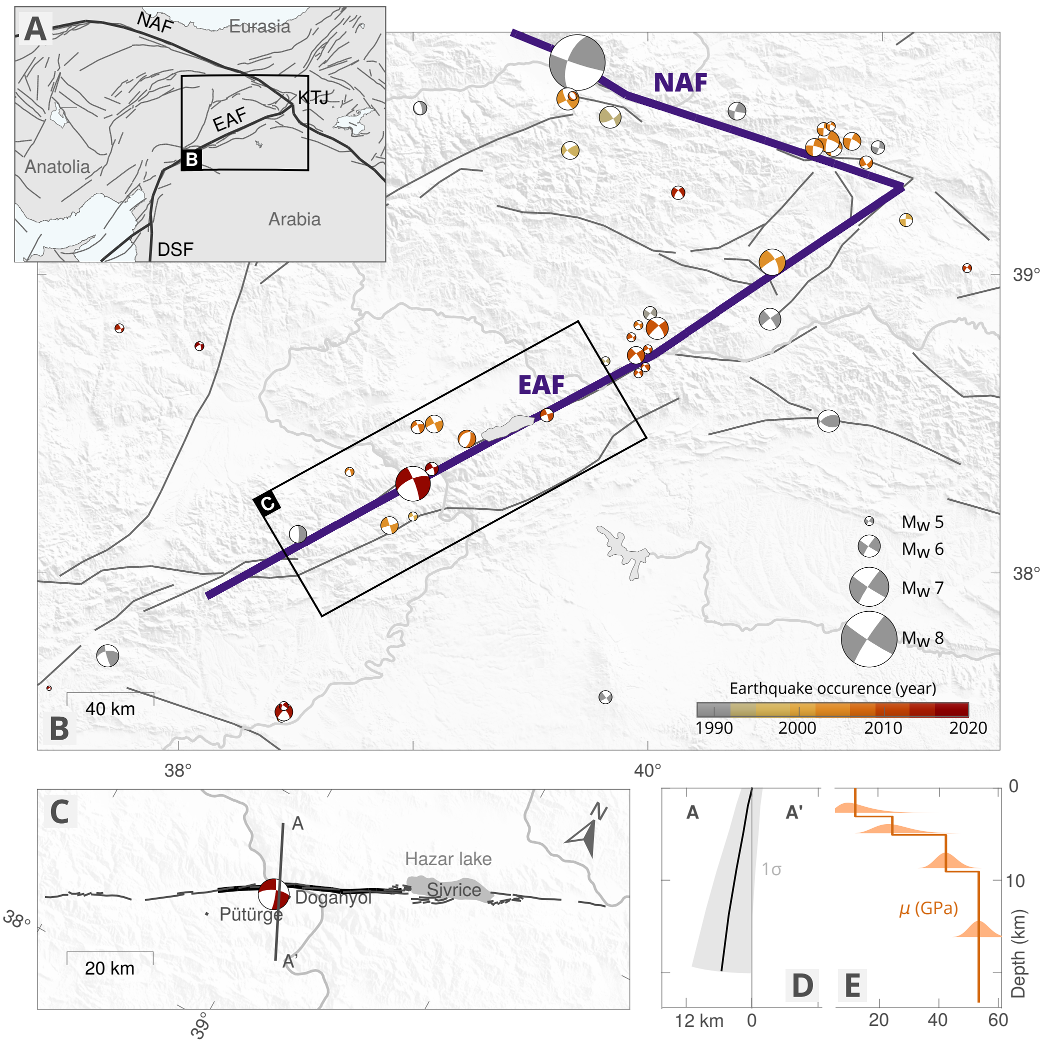

Figure 1. Tectonic setting and assumed characteristics for the Elazığ earthquake. (a) Tectonic setting of the area, plate boundaries are shown in thick black lines. East and North Anatolian Faults are labelled (EAF and NAF), as well as the Dead Sea fault (DSF) and Karlıova Triple Junction (KTJ). (b) Active fault traces (Basilic et al., 2013) and seismicity since 1976 (GCMT, Dziewonski et al., 1981) around the EAF and NAF. The Elazığ earthquake focal mechanism (GCMT) is in red. (c) Details of assumed (black) and mapped (gray) fault trace at the surface. (d) Assumed fault geometry at depth and associated uncertainty (standard deviation of 5° around the assumed dip and 1 km around the fault surface trace). (e) Assumed shear moduli with depth (derived from Maden, 2012; Ozer et al., 2019) and associated uncertainties.

1 Introduction

A large portion of Turkey is located on the Anatolian Plate (AP), which is slowly extruding westward as a result of the north-south collision between the Arabian and Eurasian tectonic plates (e.g., Mckenzie, 1970; McKenzie, 1972; McClusky et al., 2000). The westward motion of the AP is predominantly accommodated along the North and East Anatolian faults (NAF and EAF, Fig. 1). The NAF experienced a sequence of destructive earthquakes that struck within the last eighty years (e.g., A. Barka, 1996; Stein et al., 1997; Armijo et al., 1999; Şengör et al., 2005). In contrast, the EAF is generally assumed to be less active, and has only experienced small to moderate events over the last century, although large (M > 7) earthquakes have occured in the historic past (e.g., Ambraseys, 1970; Ambraseys & Jackson, 1998; Hubert-Ferrari et al., 2020).

The EAF is a left-lateral 600-km-long strike-slip fault linking the Dead Sea fault (DSF, Fig. 1) to the Karlıova Triple Junction (KTJ, Fig. 1) where it intersects with the right-lateral NAF (e.g., Yilmaz et al., 2006; Duman & Emre, 2013). The EAF has a complex geometry divided into several main segments, each of them characterized by bends, pull-apart basins or compressional structures (e.g., Duman & Emre, 2013), and also comprises multiple secondary sub-parallel and seismically active structures delineating a 50-km-wide fault zone (e.g., Bulut et al., 2012). The EAF accomodates a displacement of 9 to 15 mm/yr (Cetin et al., 2003; Reilinger et al., 2006; Cavalié & Jónsson, 2014; Bletery et al., 2020), with creep dominantly at depths greater than 5 km (Cavalié & Jónsson, 2014; Bletery et al., 2020), while shallower portions of the fault are characterized by a moderate to large inter-seismic slip deficit (Bletery et al., 2020).

The January 24 2020 M_w 6.8 earthquake ruptured the EAF between the Hazar Pull-apart Basin and the city of Pütürge (Fig. 1). Although no coseismic surface rupture has been observed, the main fault has been mapped as sinusoidal and interrupted by small bends and step-overs whose widths do not exceed a kilometer (Duman & Emre, 2013). In this study, we investigate the subsurface rupture of the Elazığ earthquake and its relationship to fault geometry and inter-seismic slip deficit. While assuming a fault structure with a realistic geometry, we also account for its inherent uncertainties, as well as uncertainties related to assumptions on the crustal structure. We adopt a Bayesian sampling approach which allows us to sample a large panel of possible slip models and to estimate the posterior uncertainty on the inverted slip distribution.

Figure 2. Observations used in thus study. (a) Surface displacement in the satellite line-of-sight (LOS) direction from a Sentinel-1 ascending interferogram (01/21/2020-01/27/2020), overlayed with coseismic GNSS offsets (Melgar et al., 2020). (b) Surface displacement from a Sentinel-1 descending interferogram (01/22/2020-01/28/2020). (c) Surface displacement from an ALOS-2 ascending interferogram (01/03/2020-01/31/2020). (d) Surface displacement from an ALOS-2 descending interferogram (03/03/2019-01/03/2020). (e) Pixel-offset surface displacement in the satellite along-track (azimuth) direction from the ALOS-2 descending pair (03/03/2019-01/03/2020). (f) Pixel-offset surface displacement in the satellite azimuth direction from the ALOS-2 ascending pair (01/03/2020-01/31/2020). The surface projection of the satellite LOS direction is positive in the ground-to-satellite direction.

2 Bayesian Inference framework

2.1 Data

We derive the earthquake surface displacement from four Synthetic Aperture Radar (SAR) interferometric pairs and two SAR pixel offsets images (summarized in Table S2 and Fig. 2). We computed two ALOS-2 ascending and descending interferograms, and two Sentinel-1 ascending and descending interferograms. Copernicus Sentinel-1 data have been acquired by the European Space Agency (ESA) and processed with the NSBAS soft-

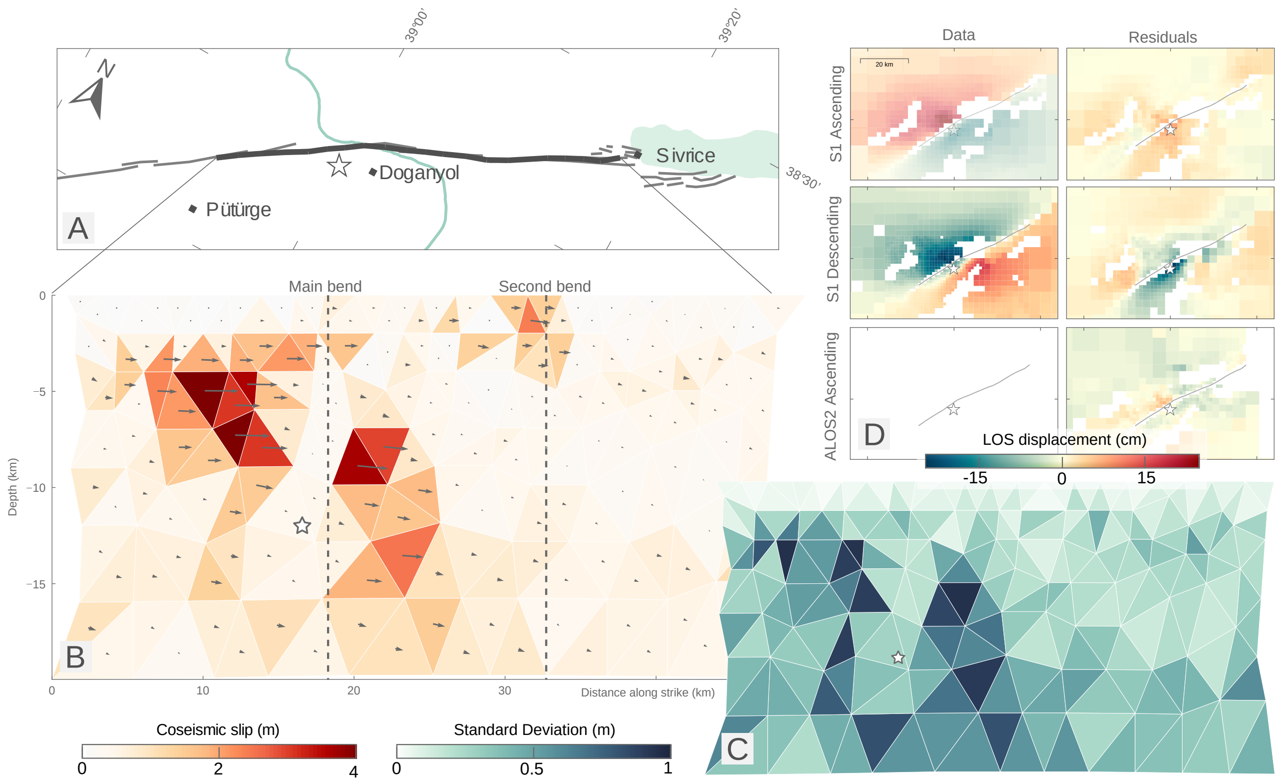

Figure 3. Inferred average slip model and associated posterior uncertainty for the Elazığ earthquake. (a) Map view of the fault trace and local setting, the epicenter is the white star. (b) Depth view of the average total slip amplitudes and directions. (c) Standard deviation of the inferred strike-slip parameters. (d) Observed and predicted surface displacement in the LOS direction from Sentinel-1 ascending and descending, and ALOS-2 ascending InSAR.

3 Results

We infer primarily strike-slip fault slip (Fig. 3). Most of the slip is imaged around the main bend (localized around the city of Doganyol, Fig. 3a). The maximum slip amplitudes (up to 4 m) are reached within two slip patches located around the main bend and from 2 to 10 km depth. Associated posterior uncertainty for these patches can reach up to ∼1 m for highest amplitudes (Fig. 3c). The westernmost slip patch extends down to greater depths (7 - 15 km) with moderate slip amplitudes of ∼2 m. At depth, the posterior model uncertainty reaches up to 1 m. The posterior marginal distributions all show well-delineated Gaussian shapes (Fig. S2), even for the smallest slip amplitudes. The posterior PDFs on subfaults in between these two main slip patches indicate well resolved very low slip amplitudes (Fig. S2), suggesting that the two patches are disconnected (Fig. 3c).

One other narrow slip patch can be observed west of the main bend, at the location of the second bend. Slip is imaged from the surface to 4-km-depth, with maximum amplitudes reaching 2.5 m at the surface, and with relatively small posterior uncertainty. This patch is not connected with the main slip patches, and does not seem to correspond to any $M_w > 4$ aftershock (relocated by Melgar et al., 2020; Pousse-Beltran et al., 2020). This slip may be coseismic or afterslip (given that the InSAR data span a period up to one month after the mainshock).

Observations are well fit by the predictions of our model (Figs. 3(d), S4, S5, S6 and S7 for the InSAR and GNSS data respectively), within the assumed uncertainties and possible remaining noise (in particular for the pixel-offset data). Accounting for epistemic uncertainties mitigates overfitting (Ragon et al., 2018). Residuals are expected to be larger than if epistemic biases are neglected. The descending interferograms present larger residuals (Figs. S4, S5, S6) because the assumed fault geometry is primarily constrained by ascending data, and the descending imaging geometry is not oriented favorably.

We also infer the slip distribution of the Elazığ earthquake assuming a planar fault structure dipping of 85° towards the north and embedded within a homogeneous half space, without introducing any epistemic uncertainty (Fig S8). Unlike our preferred model, the slip is concentrated in a single shallow and extended slip patch with low posterior uncertainty. Highest amplitudes (up to 3.5 m) are reached above the main bend, from 1.5 to 9 km depth. Low slip values are inferred at depths greater than 10 km and lower than 1.5 km. Some slip is also inferred around the second bend. As expected, the fit of the predicted displacement to the observations is good (Figs. S9, S10, S11 and S12), and slightly better than with our preferred inference.

4 Discussion and Conclusion

4.1 A stochastic view of the 2020 Elazığ coseismic rupture

Assuming a realistic fault geometry and crustal structure, and accounting for related epistemic uncertainties, we estimate the slip distribution of the 2020 Elazığ earthquake with a Bayesian inference approach. We show that the coseismic rupture affects almost the full width of the Pütürge-Sivrice segment, down to 15 km depth. Two disconnected slip patches host most of the slip: one patch extends from ~ 2.5 to ~ 12 km depth east of the main bend, reaching up to 4 m in amplitude, while the second extends

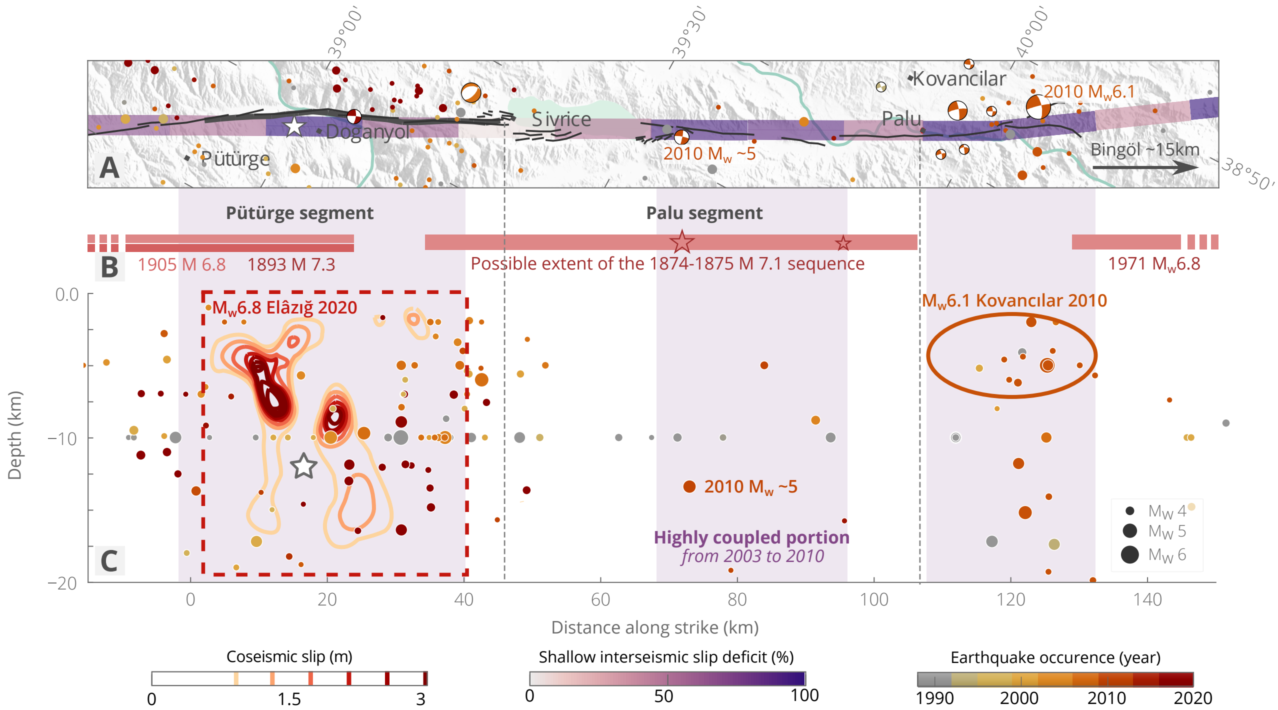

Figure 4. Comparison between the spatial distributions of the 2020 Elazığ earthquake rupture, historical earthquakes, and highly coupled sections of the EAF. (A) Map view of three segments the East Anatolian Fault (black lines), overlayed with historical and recent seismicity from 1900 to January 2020 (Retrieved from AFAD, 2020; NEIC, 2020), shallow interseismic slip deficit (Bletery et al., 2020) and our assumed fault trace for the 2020 Elazığ event (thick black line). (B) Possible rupture extents for the 4 most recent $M_w > 6.5$ earthquakes that struck the mapped segments of the EAF before the Elazığ event, inferred from Ambraseys (1989); Hubert-Ferrari et al. (2020). Red stars denote the locations of the mainshock and aftershock of the 1874 sequence (Ambraseys, 1989). Fault segments of the central EAF are indicated, from Duman and Emre (2013). (C) Depth extent of the slip amplitude inferred for the 2020 Elazığ event (Fig. 3), along with the highly coupled sections of the EAF between 2003 and 2010 (Bletery et al., 2020), and the possible extent of the 2010 M_w 6.1 Kovancılar earthquake estimated from the spatial coverage of aftershocks and basic scaling laws (Wells & Coppersmith, 1994; Tan et al., 2011), as well as historical and recent seismicity from 1900 to January 2020.

down to 15-km-depth just west of the main bend (Fig. 3). A large shallow slip (0-5 km, 2.5 m in amplitude) is also imaged around the second bend. Although the location of the epicenter, as estimated from different institutions and authors (e.g., Jamalreyhani et al., 2020), comes with a few kilometers uncertainty, it is probably located around the main bend. Our inferred model thus suggests the rupture of the Elazığ earthquake is bilateral, starting at a geometrical complexity and propagating on both sides.

The inferred slip distribution changes significantly if we assume a planar fault embedded in a homogeneous crust and we neglect uncertainties stemming from the assumption of a simplified Earth interior. In particular, a single and shallower slip patch is inferred above the epicenter, no slip larger than 50 cm being imaged above 2 km, or larger than 80 cm below 10 km depth. The slip deficit imaged when assuming a simplified forward model suggests that the pronounced shallow slip deficit observed by Pousse-Beltran et al. (2020) may be an artifact deriving from modeling choices, as proposed by Xu et al. (2016) and Ragon et al. (2018).

Our estimates of the pattern of fault slip differ from other estimates based on similar data (e.g., Melgar et al., 2020; Pousse-Beltran et al., 2020; Cheloni & Akinci, 2020). While our preferred model is very different from Pousse-Beltran et al. (2020), it shares some characteristics with the preferred one of Melgar et al. (2020), especially for the location of largest slip and the overall shape of the ruptured areas, surrounding the epicenter. Melgar et al. (2020) preferred model being primarily driven by high-rate GNSS data and assuming a 1D crustal structure, these shared characteristics suggest that assuming a layered crustal model is necessary to infer robust slip estimates in this region.

4.2 Structurally driven slip on the Pütürge segment

Fault segmentation and bends are thought to act as geometric barriers that can influence, or even drive, rupture initiation, termination and propagation (e.g., G. King & Nabelek, 1985; A. A. Barka & Kadinsky-Cade, 1988; Wesnousky, 2006; Duan & Oglesby, 2005; Aochi et al., 2002; Perrin et al., 2016). Similarly, creeping sections might act as barriers to earthquake propagation (e.g., G. C. P. King, 1986; Chlieh et al., 2008; Perfettini et al., 2010; Kaneko et al., 2010).

The coseismic rupture of the Elazığ earthquake started at the location of the main bend of this portion of the EAF (refer to Fig. 3, Melgar et al., 2020; Jamalreyhani et al., 2020). Peak slip amplitudes and most of the slip are located on both sides of this bend, which also acts as a barrier, in particular at depth, where well-resolved low slip values separate the two main slip patches. The location of the main bend also corresponds to the portion of the EAF that shows maximum shallow interseismic slip deficit (Fig. 4). Inferred slip partly overlays this portion of maximum slip deficit, but the coseismic rupture also extends over moderately coupled regions (30-40%) at greater depths (from 8 to 15-km-depth). The second bend, to the northeast of the main bend (Fig. 3), is also surrounded by large slip amplitudes at shallow depths.

Slip slowly decreases towards Lake Hazar (Fig. 4). Aftershocks activity also declines abruptly at the basin boundary (Melgar et al., 2020; Jamalreyhani et al., 2020). The pull-apart basin hosting Lake Hazar might thus have acted as a geometrical barrier to the ruptured asperity (as also observed for the Haiyuan fault, China, Liu-Zeng et al., 2007; Jolivet et al., 2013).

Altogether, these observations suggest that the distribution of subsurface fault slip during the Elazığ earthquake may largely reflect complexities in the fault geometry. The main fault bend is not prone to aseismic slip (at least at shallow depths), and it likely triggered the rupture. Both bends might have favored seismic rupture and large coseismic slip amplitudes. The main bend might also have acted as a barrier to rupture propagation, similarly to the structure responsible for the pull-apart basin of Lake Hazar. The deepest imaged slip patch, down to 15-km-depth, confirms that the seismogenic depth is deeper than 10 km for the central EAF (Bulut et al., 2012). Our results do not seem to corroborate the shallow locking depth (full creep below 5 km) inferred by Cavalié and Jónsson (2014). This behavior appears similar to the NAF, where large earthquakes occur on faults also prone to aseismic slip (Cakir et al., 2005, 2014; Schmittbuhl et al., 2016).

4.3 Seismic potential of the Palu segment

From Pütürge to Bingöl, interseismic slip deficit at shallow depths varies along strike, as inferred from geodetic data from 2003 to 2010 (Bletery et al., 2020, Fig. 4, the city of Bingöl is located just out of the map). Three main sections of large shallow interseismic slip deficit (>70%) are clearly distinct: one on the Pütürge segment, another on the Palu segment, and a last one west of the city of Palu. Before the Elazığ event, this portion of the EAF was struck by 4 large earthquakes in the last 200 years. Two M $\sim$ 6.8

and M $\sim$ 7.3 occured west of Lake Hazar in 1893 and 1905 (Ambraseys, 1989). In 1874-1875, a sequence of two M $\sim$ 7.1 and M $\sim$ 6.7 likely struck the region between Sivrice and Palu (Ambraseys, 1989; Cetin et al., 2003; Hubert-Ferrari et al., 2017). East of the locality of Palu, the region around the city of Bingöl was affected by a M_w 6.8 in 1971 (Ambraseys, 1989; Ambraseys & Jackson, 1998).

Slip deficit has accumulated on the EAF since these recent historical ruptures, and the newly coupled portions (from 2003 to 2010) are preferably located in between the historically ruptured segments (Bletery et al., 2020). The 2010 M_w 6.1 earthquake that occurred near Kovancılar (Akkar et al., 2011) appears to have filled the possible seismic gap between the 1874 sequence and the 1971 Bingöl event (Fig. 4B). Similarly, the extent of the Elazığ rupture well overlays with a highly coupled portion of the EAF, and it may have filled a possible gap between the 1893/1905 earthquakes and the 1874 sequence (Melgar et al., 2020; Duman & Emre, 2013).

Although the portions of the EAF that have been affected by the Elazığ and Kovancılar events show seismic activity in the 20 years preceding these events, the Palu segment is characterized by relatively low seismic activity (Fig. 4). Together with the low slip deficit at depth (or shallow locking depth, Cavalié & Jónsson, 2014; Bletery et al., 2020), the lack of seismicity suggests that this segment is creeping. However, this segment also shows large interseismic slip deficit in its shallow portion ($<$ 5-km-depth), and at greater depths even larger than for the Pütürge segment (before the 2020 event, Bletery et al., 2020). Ground shaking maps derived from press reports and testimonies suggest the 1874 sequence likely initiated at depth just west of Lake Hazar (Ambraseys, 1989), near the epicenter of a M_w $\sim$ 5 earthquake that occurred in 2010. The Palu segment is thus capable of producing large earthquakes. Cheloni and Akinci (2020) also suggest that the Elazığ event led to an increase in the Coulomb stress of the Palu segment. Altogether, these observations suggest that the Palu segment of the central EAF is likely seismogenic.

Acknowledgments

We are very grateful to Diego Melgar and Brendan Crowell who calculated and provided the GNSS offsets for the coseismic deformation, and their relocated aftershocks catalog, which are both available in Melgar et al. (2020). GNSS data were made available from the Turkish National Permanent GNSS/RTK Network (TUSAGA-Aktif/CORS-TR administrated by General Directorate of Land Registry and Cadastre-TKGM and General Directorate of Mapping-HGM, Ankara, Turkey). Initial aftershocks and phase-arrival catalog has been provided by the Disaster and Emergency Management Presidency of Turkey (AFAD, 2020) for the period 24 January 2020 11 February 2020, and historical/background seismicity catalog was provided by BU-KOERI (`http://www.koeri.boun.edu.tr/sismo/2/en/`) for Turkey from 1992 to 2020. This work contains modified Copernicus data from the Sentinel-1A and -1B satellites provided by the European Space Agency (ESA) that are accessible at `earth.esa.int/eogateway/`. Original ALOS-2 data and products are copyright JAXA and provided under JAXA ALOS Research Announcement 6 (RA6) project 3278, and will be made available upon acceptance at `aria-share.jpl.nasa.gov`. The Bayesian simulations were performed with the AlTar2 package (`github.com/AlTarFramework/altar`). The Classic Slip Inversion (CSI, `github.com/jolivetr/csi`) Python library (Jolivet et al., 2014) was used to build inputs for the Bayesian algorithm, in particular to compute Green's functions. The python module PyDistMesh has been used to build the fault geometry (Persson & Strang, 2004). Figures were generated with the Matplotlib and Seaborn (`doi:10.5281/zenodo.1313201`) Python libraries and with the Generic Mapping Tools library (Wessel et al., 2019). MS was partially supported by the National Aeronautics and Space Administration under Grant No. 80NSSC19K1499. EF was partially supported by the National Aeronautics and Space Administration Earth Surface and Interior focus area under Grant No. 80NM0018D0004. QB work has been supported by the French government, through the UCA JEDI Investments in the Future project managed by the National Research Agency (ANR) ANR-15-IDEX-01, the ANR S5 Grant No. ANR-19-CE31-0003, and the ANR JCJC E-POST Grant No. ANR-14-CE03-002-01JCJC.

References

AFAD. (2020). *AFAD Earthquake catalogue (1900–Feb 2020), Prime Ministry, Disaster and Emergency Management Pres-.* https://deprem.afad.gov.tr/depremkatalogu?lang=en#.

Akkar, S., Aldemir, A., Askan, A., Bakır, S., Canbay, E., Demirel, İ. O., ... Yenier, E. (2011). 8 March 2010 Elazığ-Kovancılar (Turkey) Earthquake: Observations on Ground Motions and Building Damage. *Seismological Research Letters*, *82*(1), 42–58. doi: 10.1785/gssrl.82.1.42

Ambraseys, N. N. (1970). Some characteristic features of the Anatolian fault zone.

Tectonophysics, *9*(2), 143–165. doi: 10.1016/0040-1951(70)90014-4

Ambraseys, N. N. (1989). Temporary seismic quiescence: SE Turkey. *Geophysical Journal International*, *96*(2), 311–331. doi: 10.1111/j.1365-246X.1989.tb04453.x

Ambraseys, N. N., & Jackson, J. A. (1998). Faulting associated with historical and recent earthquakes in the Eastern Mediterranean region. *Geophysical Journal International*, *133*(2), 390–406. doi: 10.1046/j.1365-246X.1998.00508.x

Aochi, H., Madariaga, R., & Fukuyama, E. (2002). Effect of normal stress during rupture propagation along nonplanar faults. *Journal of Geophysical Research: Solid Earth*, *107*(B2), ESE 5-1-ESE 5-10. doi: 10.1029/2001JB000500

Armijo, R., Meyer, B., Hubert, A., & Barka, A. (1999). Westward propagation of the North Anatolian fault into the northern Aegean: Timing and kinematics. *Geology*, *27*(3), 267–270. doi: 10.1130/0091-7613(1999)027⟨0267:WPOTNA⟩2.3.CO;2

Barka, A. (1996). Slip distribution along the North Anatolian fault associated with the large earthquakes of the period 1939 to 1967. *Bulletin of the Seismological Society of America*, *86*(5), 1238–1254.

Barka, A. A., & Kadinsky-Cade, K. (1988). Strike-slip fault geometry in Turkey and its influence on earthquake activity. *Tectonics*, *7*(3), 663–684. doi: 10.1029/TC007i003p00663

Basilic, R., Kastelic, V., Demircioglu, M. B., Garcia Moreno, D., Nemser, E. S., Petricca, P., … Wössner, J. (2013). The European Database of Seismogenic Faults (EDSF) compiled in the framework of the Project SHARE. doi: 10.6092/INGV.IT-SHARE-EDSF

Beresnev, I. A. (2003). Uncertainties in Finite-Fault Slip Inversions: To What Extent to Believe? (A Critical Review). *Bulletin of the Seismological Society of America*, *93*(6), 2445–2458. doi: 10.1785/0120020225

Bletery, Q., Cavalié, O., Nocquet, J.-M., & Ragon, T. (2020). Distribution of Interseismic Coupling Along the North and East Anatolian Faults Inferred From InSAR and GPS Data. *Geophysical Research Letters*, *47*(16), e2020GL087775. doi: 10.1029/2020GL087775

Bulut, F., Bohnhoff, M., Eken, T., Janssen, C., Kılıç, T., & Dresen, G. (2012). The East Anatolian Fault Zone: Seismotectonic setting and spatiotemporal characteristics of seismicity based on precise earthquake locations. *Journal of Geophysical Research: Solid Earth*, *117*(B7). doi: 10.1029/2011JB008966

Cakir, Z., Akoglu, A. M., Belabbes, S., Ergintav, S., & Meghraoui, M. (2005). Creeping along the Ismetpasa section of the North Anatolian fault (Western Turkey): Rate and extent from InSAR. *Earth and Planetary Science Letters*, *238*(1), 225–234. doi: 10.1016/j.epsl.2005.06.044

Cakir, Z., Ergintav, S., Akoğlu, A. M., Çakmak, R., Tatar, O., & Meghraoui, M. (2014). InSAR velocity field across the North Anatolian Fault (eastern Turkey): Implications for the loading and release of interseismic strain accumulation. *Journal of Geophysical Research: Solid Earth*, *119*(10), 7934–7943. doi: 10.1002/2014JB011360

Causse, M., Cotton, F., & Mai, P. M. (2010). Constraining the roughness degree of slip heterogeneity. *Journal of Geophysical Research: Solid Earth*, *115*(B5). doi: 10.1029/2009JB006747

Cavalié, O., & Jónsson, S. (2014). Block-like plate movements in eastern Anatolia observed by InSAR. *Geophysical Research Letters*, 26–31. doi: 10.1002/2013GL058170@10.1002/(ISSN)1944-8007.GRLeditorhghlts2014

Cetin, H., Güneyli, H., & Mayer, L. (2003). Paleoseismology of the Palu–Lake Hazar segment of the East Anatolian Fault Zone, Turkey. *Tectonophysics*, *374*(3), 163–197. doi: 10.1016/j.tecto.2003.08.003

Cheloni, D., & Akinci, A. (2020). Source modelling and strong ground motion simulations for the January 24, 2020, Mw 6.8 Elazığ earthquake, Turkey. *Geophysical Journal International*. doi: 10.1093/gji/ggaa350

Chlieh, M., Avouac, J. P., Sieh, K., Natawidjaja, D. H., & Galetzka, J. (2008). Heterogeneous coupling of the Sumatran megathrust constrained by geodetic and paleogeodetic measurements. *Journal of Geophysical Research: Solid Earth*, *113*(B5). doi: 10.1029/2007JB004981

Diao, F., Wang, R., Aochi, H., Walter, T. R., Zhang, Y., Zheng, Y., & Xiong, X. (2016). Rapid kinematic finite-fault inversion for an Mw 7+ scenario earthquake in the Marmara Sea: An uncertainty study. *Geophysical Journal International*, *204*(2), 813–824. doi: 10.1093/gji/ggv459

Doin, M.-P., Lodge, F., Guillaso, S., Jolivet, R., Lasserre, C., Ducret, G., … Pinel, V. (2012). Presentation Of The Small Baseline NSBAS Processing Chain On A

Case Example: The ETNA Deformation Monitoring From 2003 to 2010 Using ENVISAT Data. , *697*, 98.

Du, Y., Aydin, A., & Segall, P. (1992). Comparison of various inversion techniques as applied to the determination of a geophysical deformation model for the 1983 Borah Peak earthquake. *Bulletin of the Seismological Society of America*, *82*(4), 1840–1866.

Duan, B., & Oglesby, D. D. (2005). Multicycle dynamics of nonplanar strike-slip faults. *Journal of Geophysical Research: Solid Earth*, *110*(B3). doi: 10.1029/2004JB003298

Duman, T. Y., & Emre, Ö. (2013). The East Anatolian Fault: Geometry, segmentation and jog characteristics. *Geological Society, London, Special Publications*, *372*(1), 495–529. doi: 10.1144/SP372.14

Duputel, Z., Agram, P. S., Simons, M., Minson, S. E., & Beck, J. L. (2014). Accounting for prediction uncertainty when inferring subsurface fault slip. *Geophysical Journal International*, *197*(1), 464–482. doi: 10.1093/gji/ggt517

Dziewonski, A. M., Chou, T.-A., & Woodhouse, J. H. (1981). Determination of earthquake source parameters from waveform data for studies of global and regional seismicity. *Journal of Geophysical Research: Solid Earth*, *86*(B4), 2825–2852. doi: 10.1029/JB086iB04p02825

Gallovič, F., Imperatori, W., & Mai, P. M. (2015). Effects of three-dimensional crustal structure and smoothing constraint on earthquake slip inversions: Case study of the Mw6.3 2009 L'Aquila earthquake. *Journal of Geophysical Research: Solid Earth*, *120*(1), 2014JB011650. doi: 10.1002/2014JB011650

Garcia Moreno, D., Hubert, A., Moernaut, J., Fraser, J., Boes, X., Van Daele, M., … De Batist, M. (2011). Structure and evolution of Lake Hazar pull-apart Basin along the East Anatolian Fault. *Basin Research*, *23*. doi: 10.1111/j.1365-2117.2010.00476.x

Hartzell, S., Liu, P., Mendoza, C., Ji, C., & Larson, K. M. (2007). Stability and Uncertainty of Finite-Fault Slip Inversions: Application to the 2004 Parkfield, California, Earthquake. *Bulletin of the Seismological Society of America*, *97*(6), 1911–1934. doi: 10.1785/0120070080

Hubert-Ferrari, A., Lamair, L., Hage, S., Schmidt, S., Çağatay, M. N., & Avşar, U. (2020). A 3800 yr paleoseismic record (Lake Hazar sediments, eastern Turkey):

Implications for the East Anatolian Fault seismic cycle. *Earth and Planetary Science Letters*, *538*, 116152. doi: 10.1016/j.epsl.2020.116152

Hubert-Ferrari, A., El-Ouahabi, M., Garcia-Moreno, D., Avşar, U., Altınok, S., Schmidt, S., ... Çağatay, M. N. (2017). Earthquake imprints on a lacustrine deltaic system: The Kürk Delta along the East Anatolian Fault (Turkey). *Sedimentology*, *64*(5), 1322–1353. doi: 10.1111/sed.12355

Jamalreyhani, M., Büyükakpınar, P., Cesca, S., Dahm, T., Sudhaus, H., Rezapour, M., ... Heimann, S. (2020). Seismicity related to the eastern sector of Anatolian escape tectonic: The example of the 24 January 2020 Mw 6.77 Elazığ-Sivrice earthquake. *Solid Earth Discussions*, 1–22. doi: 10.5194/se-2020-55

Jolivet, R., Duputel, Z., Riel, B., Simons, M., Rivera, L., Minson, S. E., ... Fielding, E. J. (2014). The 2013 Mw 7.7 Balochistan Earthquake: Seismic Potential of an Accretionary Wedge. *Bulletin of the Seismological Society of America*, *104*(2), 1020–1030. doi: 10.1785/0120130313

Jolivet, R., Lasserre, C., Doin, M.-P., Guillaso, S., Peltzer, G., Dailu, R., ... Xu, X. (2012). Shallow creep on the Haiyuan Fault (Gansu, China) revealed by SAR Interferometry. *Journal of Geophysical Research: Solid Earth*, *117*(B6), B06401. doi: 10.1029/2011JB008732

Jolivet, R., Lasserre, C., Doin, M. P., Peltzer, G., Avouac, J. P., Sun, J., & Dailu, R. (2013). Spatio-temporal evolution of aseismic slip along the Haiyuan fault, China: Implications for fault frictional properties. *Earth and Planetary Science Letters*, *377-378*, 23–33. doi: 10.1016/j.epsl.2013.07.020

Kaneko, Y., Avouac, J.-P., & Lapusta, N. (2010). Towards inferring earthquake patterns from geodetic observations of interseismic coupling. *Nature Geoscience*, *3*(5), 363–369. doi: 10.1038/ngeo843

King, G., & Nabelek, J. (1985). Role of Fault Bends in the Initiation and Termination of Earthquake Rupture. *Science*, *228*(4702), 984–987. doi: 10.1126/science.228.4702.984

King, G. C. P. (1986). Speculations on the geometry of the initiation and termination processes of earthquake rupture and its relation to morphology and geological structure. *pure and applied geophysics*, *124*(3), 567–585. doi: 10.1007/BF00877216

Langer, L., Ragon, T., Sladen, A., & Tromp, J. (2020). Impact of topography on earthquake static slip estimates. *Tectonophysics*, 228566. doi: 10.1016/j.tecto.2020.228566

Liang, C., & Fielding, E. J. (2017a). Interferometry With ALOS-2 Full-Aperture ScanSAR Data. *IEEE Transactions on Geoscience and Remote Sensing*, *55*(5), 2739–2750. doi: 10.1109/TGRS.2017.2653190

Liang, C., & Fielding, E. J. (2017b). Measuring Azimuth Deformation With L-Band ALOS-2 ScanSAR Interferometry. *IEEE Transactions on Geoscience and Remote Sensing*, *55*(5), 2725–2738. doi: 10.1109/TGRS.2017.2653186

Liu-Zeng, J., Klinger, Y., Xu, X., Lasserre, C., Chen, G., Chen, W., ... Zhang, B. (2007). Millennial Recurrence of Large Earthquakes on the Haiyuan Fault near Songshan, Gansu Province, China. *Bulletin of the Seismological Society of America*, *97*(1B), 14–34. doi: 10.1785/0120050118

Lohman, R. B., & Simons, M. (2005). Some thoughts on the use of InSAR data to constrain models of surface deformation: Noise structure and data downsampling. *Geochemistry, Geophysics, Geosystems*, *6*(1), Q01007. doi: 10.1029/2004GC000841

Maden, N. (2012). One-Dimensional Thermal Modeling of the Eastern Pontides Orogenic Belt (NE Turkey). *Pure and Applied Geophysics*, *169*(1), 235–248. doi: 10.1007/s00024-011-0296-0

Mai, P. M., Schorlemmer, D., Page, M., Ampuero, J.-P., Asano, K., Causse, M., ... Zielke, O. (2016). The Earthquake-Source Inversion Validation (SIV) Project. *Seismological Research Letters*. doi: 10.1785/0220150231

McClusky, S., Balassanian, S., Barka, A., Demir, C., Ergintav, S., Georgiev, I., ... Veis, G. (2000). Global Positioning System constraints on plate kinematics and dynamics in the eastern Mediterranean and Caucasus. *Journal of Geophysical Research: Solid Earth*, *105*(B3), 5695–5719. doi: 10.1029/1999JB900351

McKenzie, D. (1972). Active Tectonics of the Mediterranean Region. *Geophysical Journal International*, *30*(2), 109–185. doi: 10.1111/j.1365-246X.1972.tb02351.x

Mckenzie, D. P. (1970). Plate Tectonics of the Mediterranean Region. *Nature*, *226*(5242), 239–243. doi: 10.1038/226239a0

Melgar, D., Ganas, A., Taymaz, T., Valkaniotis, S., Crowell, B. W., Kapetanidis, V., … Öcalan, T. (2020). Rupture kinematics of January 24, 2020 Mw 6.7 Doğanyol-Sivrice, Turkey earthquake on the East Anatolian Fault zone imaged by space geodesy. *Geophysical Journal International*. doi: 10.1093/gji/ggaa345

Minson, S. E., Simons, M., & Beck, J. L. (2013). Bayesian inversion for finite fault earthquake source models I – theory and algorithm. *Geophysical Journal International*, *194*(3), 1701–1726. doi: 10.1093/gji/ggt180

Minson, S. E., Simons, M., Beck, J. L., Ortega, F., Jiang, J., Owen, S. E., … Sladen, A. (2014). Bayesian inversion for finite fault earthquake source models – II: The 2011 great Tohoku-oki, Japan earthquake. *Geophysical Journal International*, *198*(2), 922–940. doi: 10.1093/gji/ggu170

NEIC. (2020). *NEIC Earthquake catalogue. National Earthquake Information Centre, On-line Bulletin,*. https://earthquake.usgs.gov/earthquakes/search/.

Ozer, C., Ozyazicioglu, M., Gok, E., & Polat, O. (2019). Imaging the Crustal Structure Throughout the East Anatolian Fault Zone, Turkey, by Local Earthquake Tomography. *Pure and Applied Geophysics*, *176*(6), 2235–2261. doi: 10.1007/s00024-018-2076-6

Perfettini, H., Avouac, J.-P., Tavera, H., Kositsky, A., Nocquet, J.-M., Bondoux, F., … Soler, P. (2010). Seismic and aseismic slip on the Central Peru megathrust. *Nature*, *465*(7294), 78–81.

Perrin, C., Manighetti, I., & Gaudemer, Y. (2016). Off-fault tip splay networks: A genetic and generic property of faults indicative of their long-term propagation. *Comptes Rendus Geoscience*, *348*(1), 52–60. doi: 10.1016/j.crte.2015.05.002

Persson, P.-O., & Strang, G. (2004). A Simple Mesh Generator in MATLAB. *SIAM Review*, *46*(2), 329–345. doi: 10.1137/S0036144503429121

Pousse-Beltran, L., Nissen, E., Bergman, E. A., Cambaz, M. D., Gaudreau, É., Karasözen, E., & Tan, F. (2020). The 2020 Mw 6.8 Elazığ (Turkey) Earthquake Reveals Rupture Behavior of the East Anatolian Fault. *Geophysical Research Letters*, *47*(13), e2020GL088136. doi: 10.1029/2020GL088136

Ragon, T., Sladen, A., Bletery, Q., Vergnolle, M., Cavalié, O., Avallone, A., … Delouis, B. (2019). Joint Inversion of Coseismic and Early Postseismic Slip to

Optimize the Information Content in Geodetic Data: Application to the 2009 Mw6.3 L'Aquila Earthquake, Central Italy. *Journal of Geophysical Research: Solid Earth*, *124*(10), 10522–10543. doi: 10.1029/2018JB017053

Ragon, T., Sladen, A., & Simons, M. (2018). Accounting for uncertain fault geometry in earthquake source inversions – I: Theory and simplified application. *Geophysical Journal International*, *214*(2), 1174–1190. doi: 10.1093/gji/ggy187

Ragon, T., Sladen, A., & Simons, M. (2019). Accounting for uncertain fault geometry in earthquake source inversions – II: Application to the Mw 6.2 Amatrice earthquake, central Italy. *Geophysical Journal International*, *218*(1), 689–707. doi: 10.1093/gji/ggz180

Razafindrakoto, H. N. T., & Mai, P. M. (2014). Uncertainty in Earthquake Source Imaging Due to Variations in Source Time Function and Earth Structure. *Bulletin of the Seismological Society of America*, *104*(2), 855–874. doi: 10.1785/0120130195

Reilinger, R., McClusky, S., Vernant, P., Lawrence, S., Ergintav, S., Cakmak, R., … Karam, G. (2006). GPS constraints on continental deformation in the Africa-Arabia-Eurasia continental collision zone and implications for the dynamics of plate interactions. *Journal of Geophysical Research: Solid Earth*, *111*(B5). doi: 10.1029/2005JB004051

Rosen, P. A. G. (2012). The InSAR Scientific Computing Environment. In *9th European Conference on Synthetic Aperture Radar.* Nuremberg, Germany.

Schmittbuhl, J., Karabulut, H., Lengliné, O., & Bouchon, M. (2016). Long-lasting seismic repeaters in the Central Basin of the Main Marmara Fault. *Geophysical Research Letters*, *43*(18), 9527–9534. doi: 10.1002/2016GL070505

Şengör, A., Tüysüz, O., İmren, C., Sakınç, M., Eyidoğan, H., Görür, N., … Rangin, C. (2005). The North Anatolian Fault: A New Look. *Annual Review of Earth and Planetary Sciences*, *33*(1), 37–112. doi: 10.1146/annurev.earth.32.101802.120415

Stein, R. S., Barka, A. A., & Dieterich, J. H. (1997). Progressive failure on the North Anatolian fault since 1939 by earthquake stress triggering. *Geophysical Journal International*, *128*(3), 594–604. doi: 10.1111/j.1365-246X.1997.tb05321.x

Tan, O., Pabuçcu, Z., Tapırdamaz, M. C., İnan, S., Ergintav, S., Eyidoğan, H., ... Kuluöztürk, F. (2011). Aftershock study and seismotectonic implications of the 8 March 2010 Kovancılar (Elazığ, Turkey) earthquake (MW = 6.1). *Geophysical Research Letters*, *38*(11). doi: 10.1029/2011GL047702

Tarantola, A. (2005). *Inverse Problem Theory and Methods for Model Parameter Estimation*. Society for Industrial and Applied Mathematics.

Twardzik, C., Vergnolle, M., Sladen, A., & Avallone, A. (2019). Unravelling the contribution of early postseismic deformation using sub-daily GNSS positioning —. *Scientific Reports*, *9*(1), 1775. doi: 10.1038/s41598-019-39038-z

Wells, D. L., & Coppersmith, K. J. (1994). New empirical relationships among magnitude, rupture length, rupture width, rupture area, and surface displacement. *Bulletin of the Seismological Society of America*, *84*(4), 974–1002.

Wesnousky, S. G. (2006). Predicting the endpoints of earthquake ruptures. *Nature*, *444*(7117), 358–360. doi: 10.1038/nature05275

Wessel, P., Luis, J. F., Uieda, L., Scharroo, R., Wobbe, F., Smith, W. H. F., & Tian, D. (2019). The Generic Mapping Tools Version 6. *Geochemistry, Geophysics, Geosystems*, *n/a*(n/a). doi: 10.1029/2019GC008515

Xu, X., Tong, X., Sandwell, D. T., Milliner, C. W. D., Dolan, J. F., Hollingsworth, J., ... Ayoub, F. (2016). Refining the shallow slip deficit. *Geophysical Journal International*, *204*(3), 1867–1886. doi: 10.1093/gji/ggv563

Yagi, Y., & Fukahata, Y. (2008). Importance of covariance components in inversion analyses of densely sampled observed data: An application to waveform data inversion for seismic source processes. *Geophysical Journal International*, *175*(1), 215–221. doi: 10.1111/j.1365-246X.2008.03884.x

Yilmaz, H., Over, S., & Ozden, S. (2006). Kinematics of the East Anatolian Fault Zone between Turkoglu (Kahramanmaras) and Celikhan (Adiyaman), eastern Turkey. *Earth, Planets and Space*, *58*(11), 1463–1473. doi: 10.1186/BF03352645

Zhu, L., & Rivera, L. A. (2002). A note on the dynamic and static displacements from a point source in multilayered media. *Geophysical Journal International*, *148*(3), 619–627. doi: 10.1046/j.1365-246X.2002.01610.x

Supporting Information for
"A stochastic view of the 2020 Elazığ M_w6.8 earthquake"

Théa Ragon[1], Mark Simons[1], Quentin Bletery[2], Olivier Cavalié[2], Eric Fielding[3]
[1]Seismological Laboratory, California Institute of Technology, Pasadena, CA, USA.
[2]Université Côte dAzur, IRD, CNRS, Observatoire de la Côte dAzur, Géoazur, France.
[3]Jet Propulsion Laboratory, California Institute of Technology, Pasadena, CA, USA.

Contents of this file

1. Tables S1 to S2
2. Figures S1 to S12

0094-8276/20/$5.00

Width (km)	ρ **(mg/m^3)**	**Vp (km/s)**	**Vs (km/s)**	μ **(GPa)**	Std in μ
3.0	2.20	3.5	2.33	11.9	6
2.0	2.20	5.0	3.33	24.4	5
4.0	2.65	6.0	4.00	42.4	3.5
26.0	2.85	6.5	4.33	53.4	3
0.0	5.85	7.8	5.20	77.4	3

Table S1. Assumed elastic structure and assumed uncertainties (std = standard deviation). Poisson's ratio is assumed constant for each layer.

Satellite	**Orbital direction**	**Track**	**Interferogram pair**
ALOS 2	ascending	A182	2020/01/03 - 2020/01/31
ALOS 2	descending	D077	2019/03/03 - 2020/03/01
Sentinel 1A	ascending	TA116	2020/01/21 - 2020/01/27
Sentinel 1A	descending	TD123	2020/01/22 - 2020/01/28

Table S2. Interferometric pairs used for the study of the Elazig earthquake.

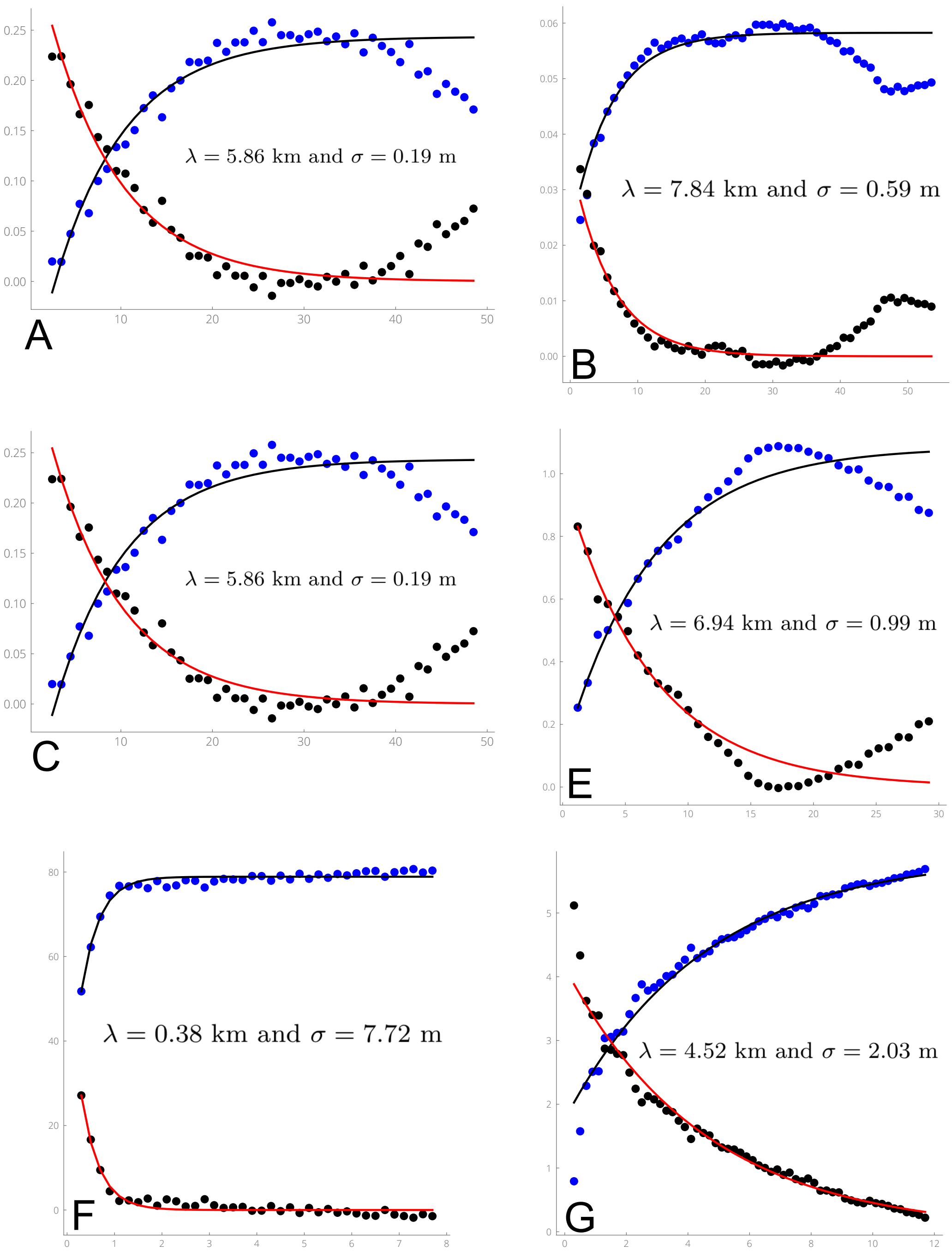

Figure S1. Empirical covariance functions (cm^2) in fonction of the distance between data points (km) for the pairs used in the study of the Elazig earthquake. A) Sentinel 1 Ascending. B) Sentinel 1 Descending. C) ALOS2 ascending. D) ALOS2 descending. E) ALOS2 descending pixel-offset. F) ALOS2 ascending pixel-offset. Radially symmetric empirical covariance functions (black points) and associated best fit exponential functions (red curve), as well as semivariograsm (black curve) are shown. For each interferogram, we compute the empirical covariance as a function of the inter-pixel distance and then fit an exponential function (Jolivet et al. 2012) such that σ and λ characterize $C(i,j) = \sigma^2 e^{-\frac{||i,j||^2}{\lambda}}$.

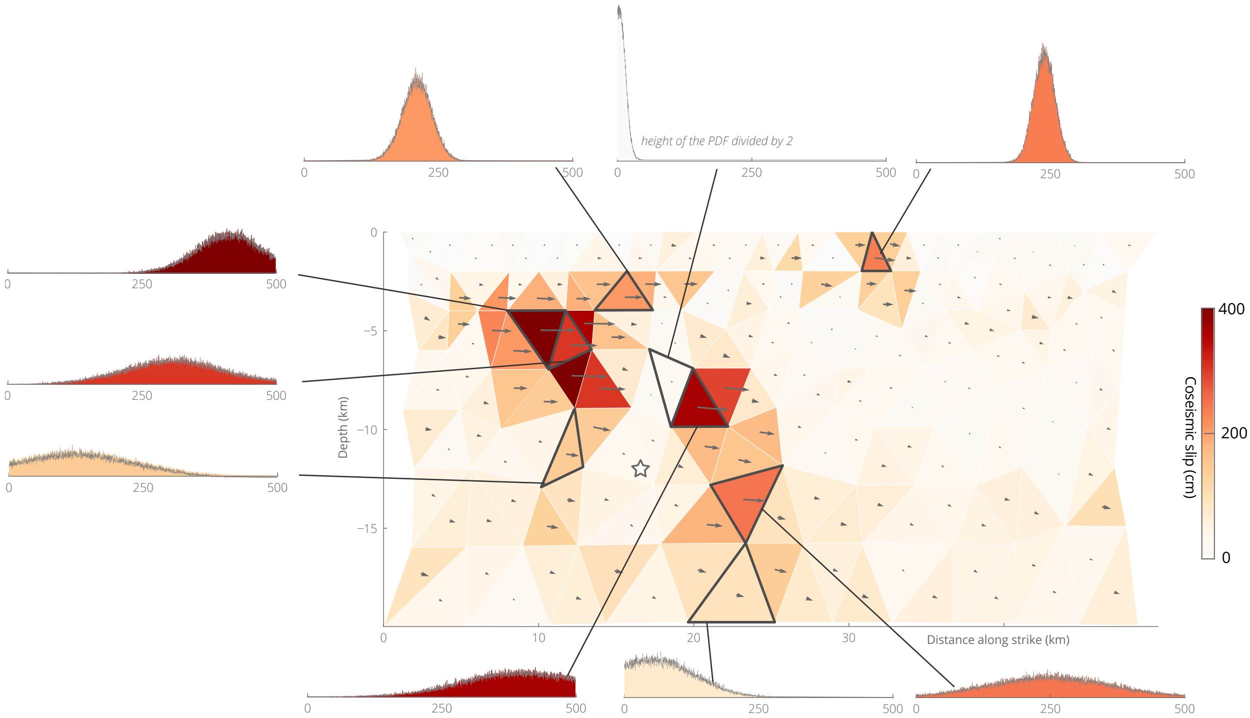

Figure S2. Posterior marginal probability density functions for selected strike-slip parameters of our preferred slip model.

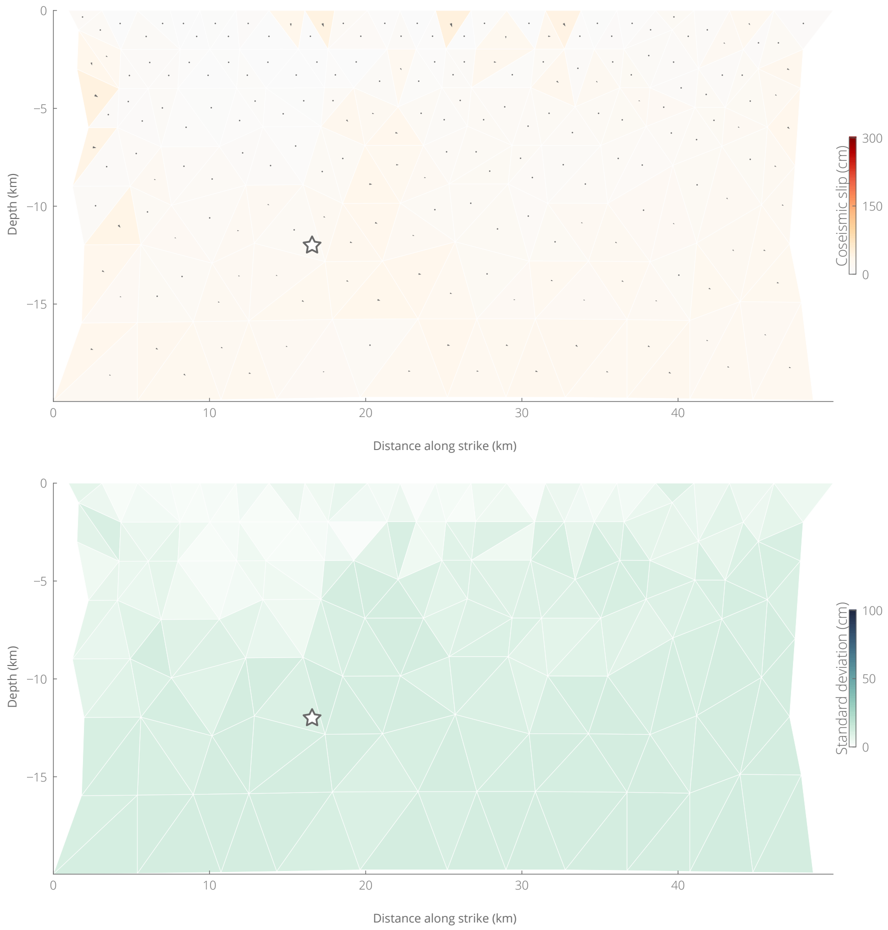

Figure S3. Inferred dip-slip amplitude (top) and associated standard deviation (bottom) for our preferred slip model.

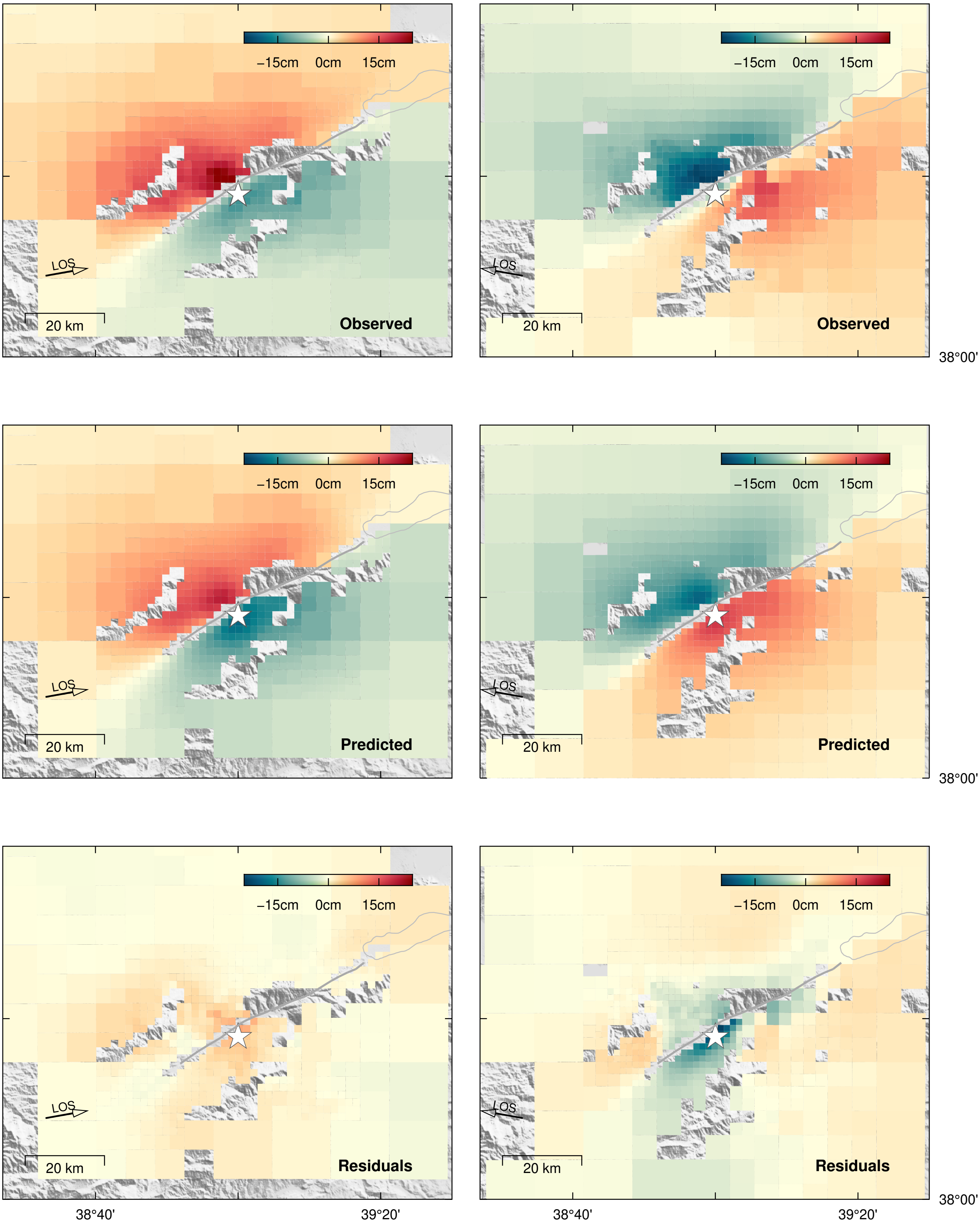

Figure S4. Observed and predicted surface displacement in the LOS direction for the Sentinel-1 ascending (left) and descending (right) interferograms. Predictions are inferred from the average model. The assumed fault trace is shown with a dark gray line.

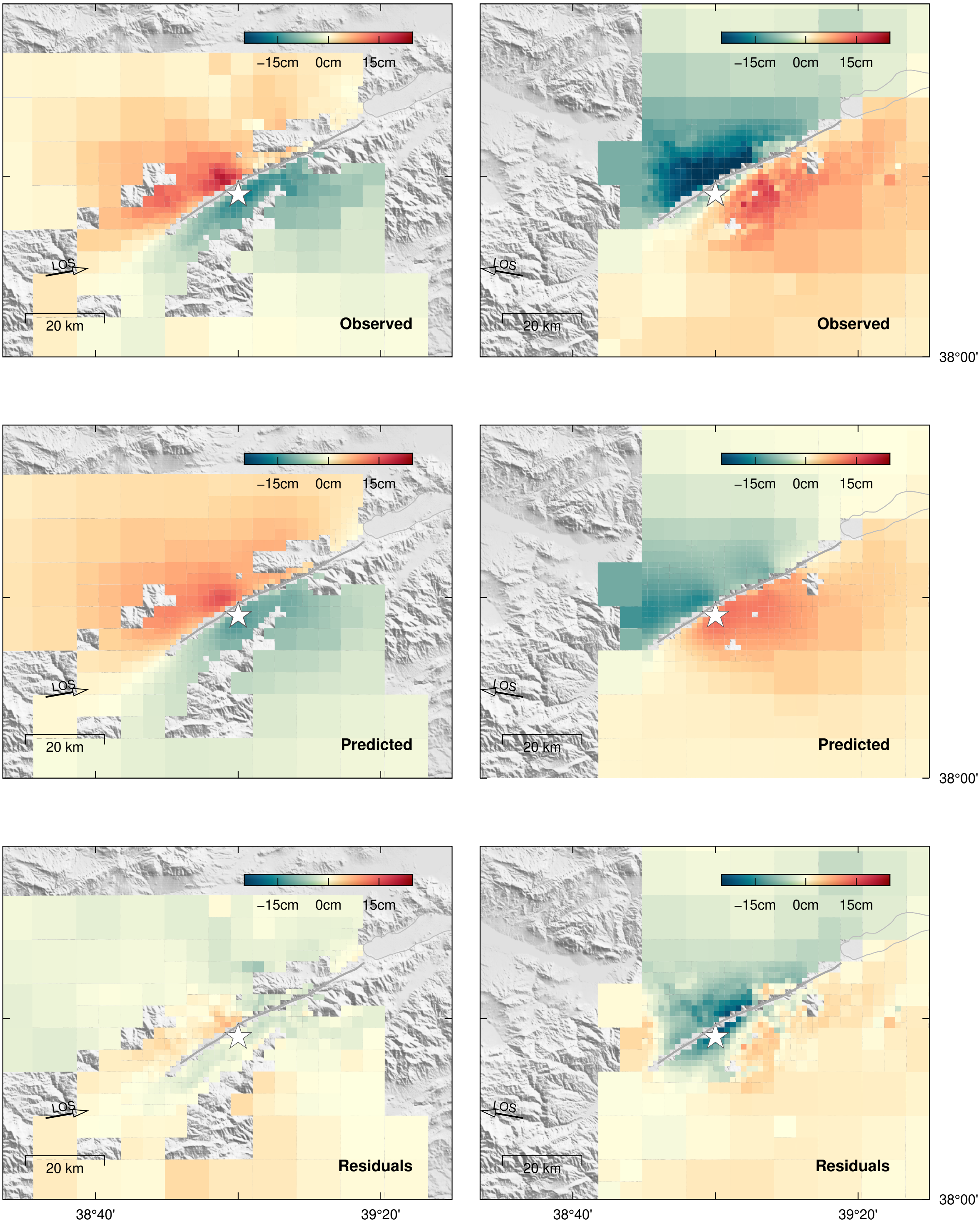

Figure S5. Observed and predicted surface displacement in the LOS direction for the ALOS 2 ascending (left) and descending (right) interferograms. Predictions are inferred from the average model. The assumed fault trace is shown with a dark gray line.

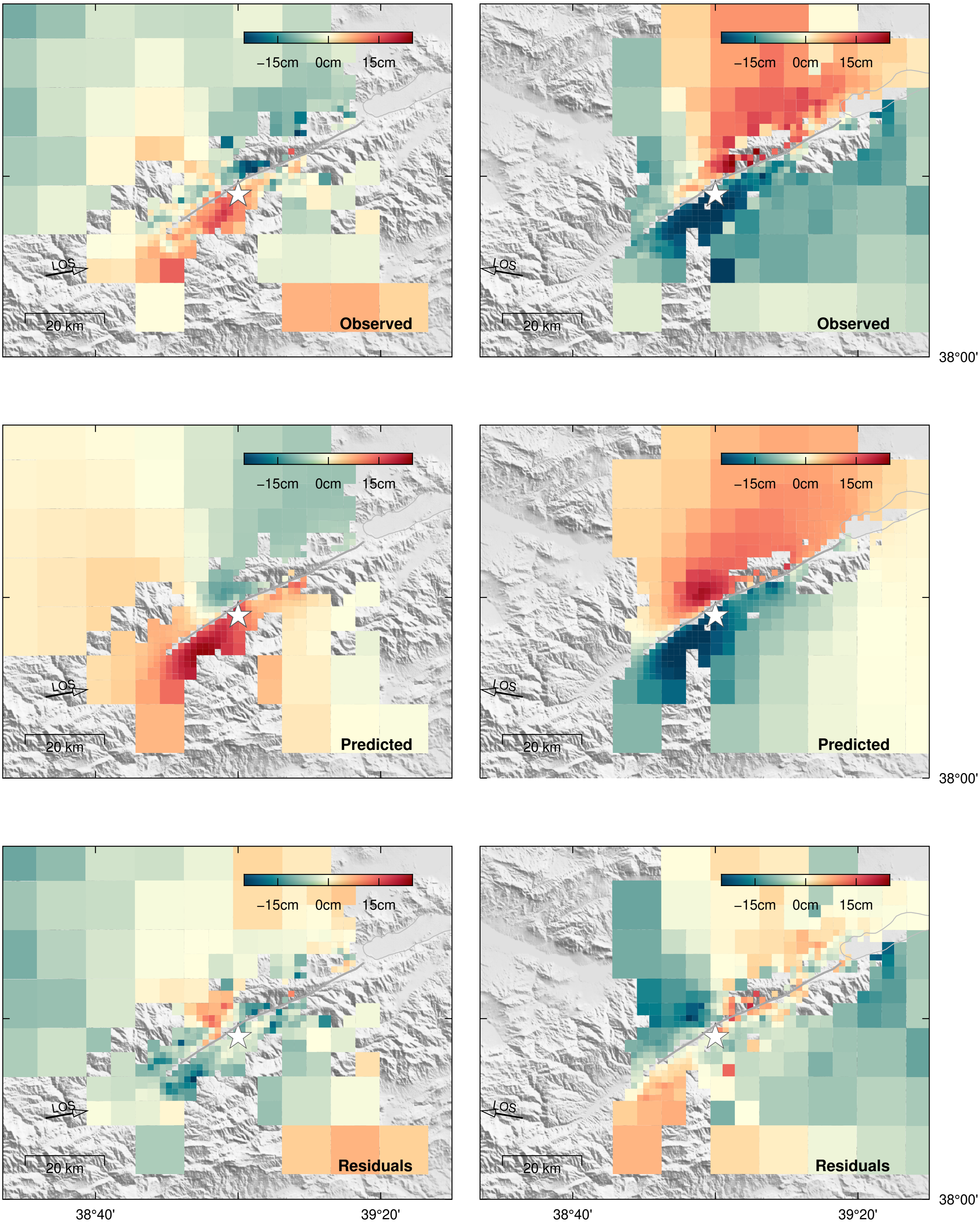

Figure S6. Observed and predicted pixel-offset surface displacement in the satellite azimuth direction for ALOS2 ascending (left) and descending (right) pairs. Predictions are inferred from the average model. The assumed fault trace is shown with a dark gray line.

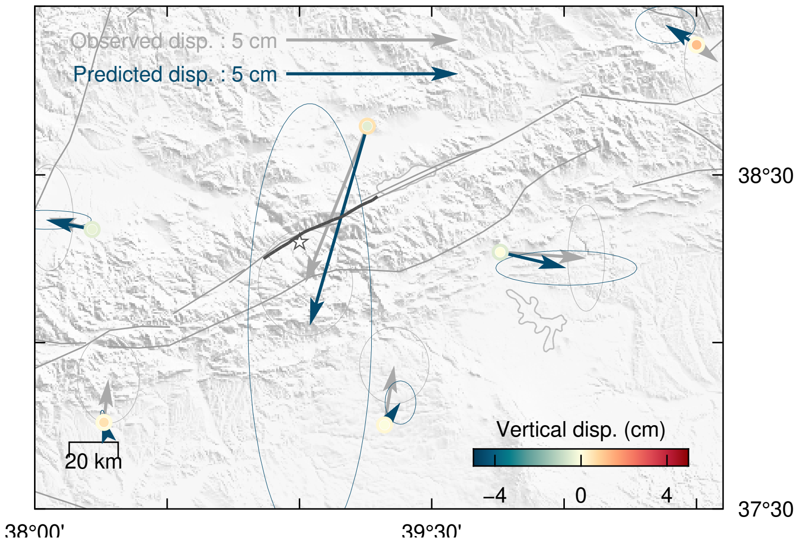

Figure S7. Observed and predicted surface displacement at the GNSS locations. Observed horizontal surface displacements are shown in gray with 90% confidence ellipses and vertical displacements as the inner amplitudes. Predicted horizontal displacements are shown in blue with 90% confidence ellipses and vertical displacements are the outer amplitudes. The assumed fault trace is shown with a dark gray line and the epicenter is the white star.

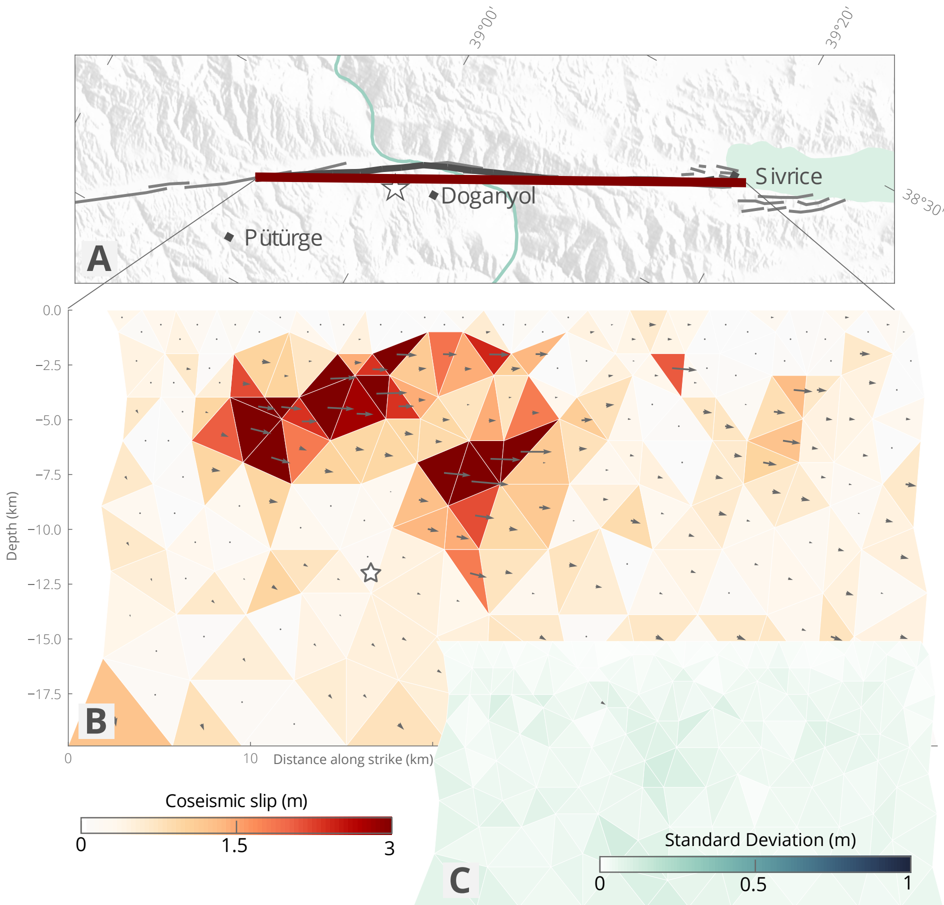

Figure S8. Inferred slip model and associated posterior uncertainty for the Elazığ earthquake, assuming a planar and vertical fault and no epistemic uncertainties. (a) Map view of the fault trace and local setting, the epicenter is the white star. (b) Depth view of the inferred total slip amplitudes and directions. (c) Standard deviation of the inferred strike-slip parameters.

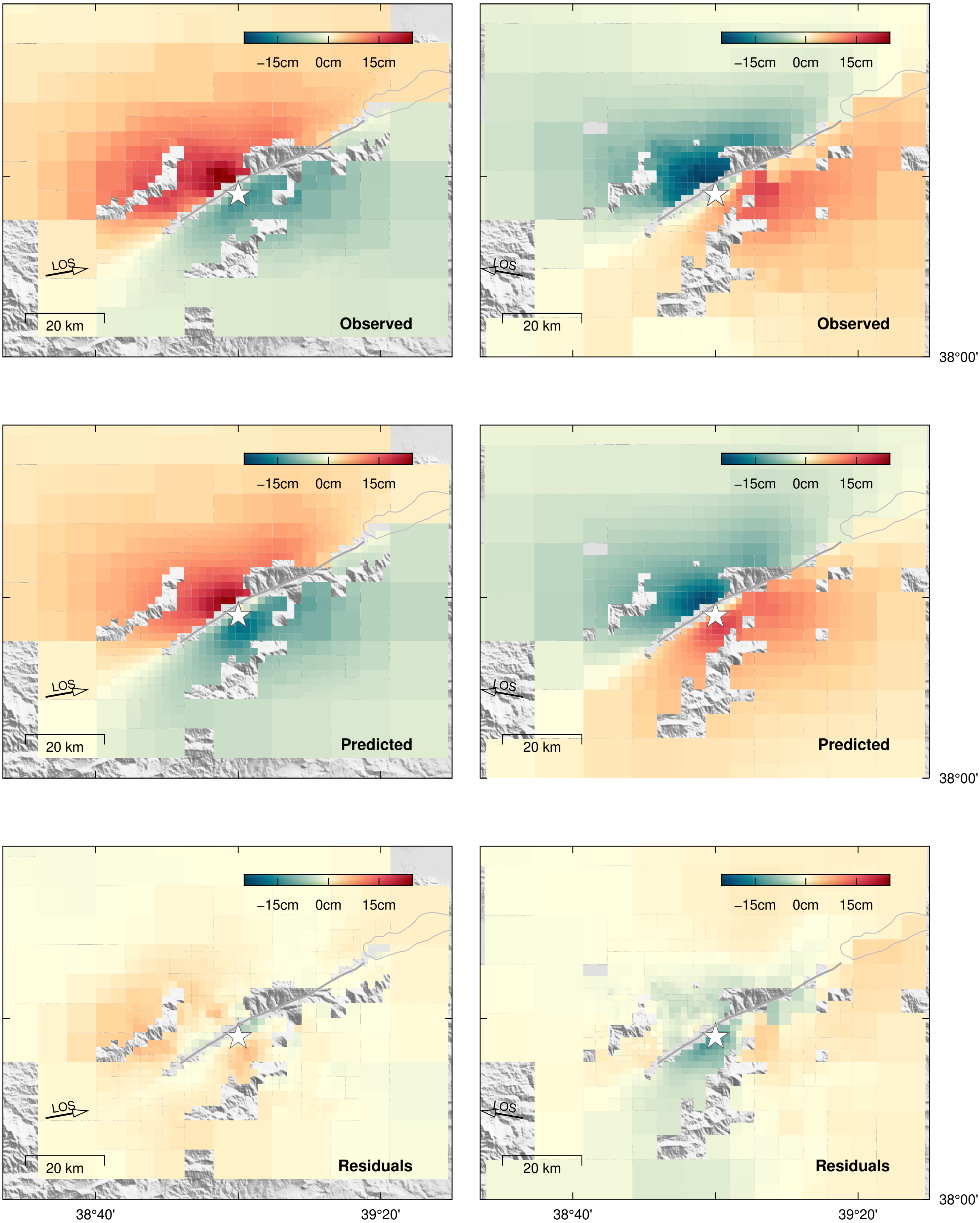

Figure S9. Observed and predicted surface displacement in the LOS direction for the Sentinel-1 ascending (left) and descending (right) interferograms. Predictions are inferred from the average model. The assumed fault trace is shown with a dark gray line.

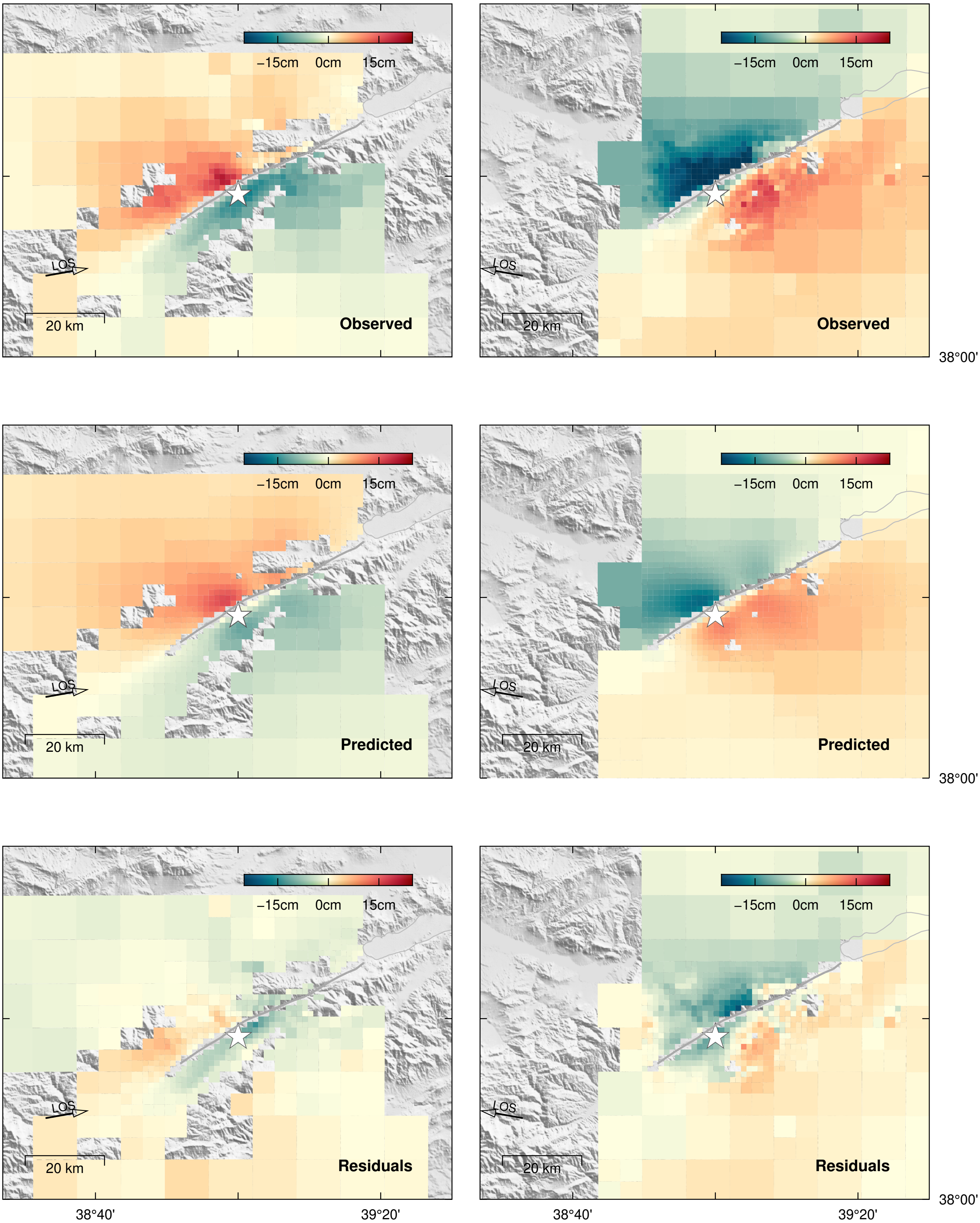

Figure S10. Observed and predicted surface displacement in the LOS direction for the ALOS 2 ascending (left) and descending (right) interferograms. Predictions are inferred from the average model. The assumed fault trace is shown with a dark gray line.

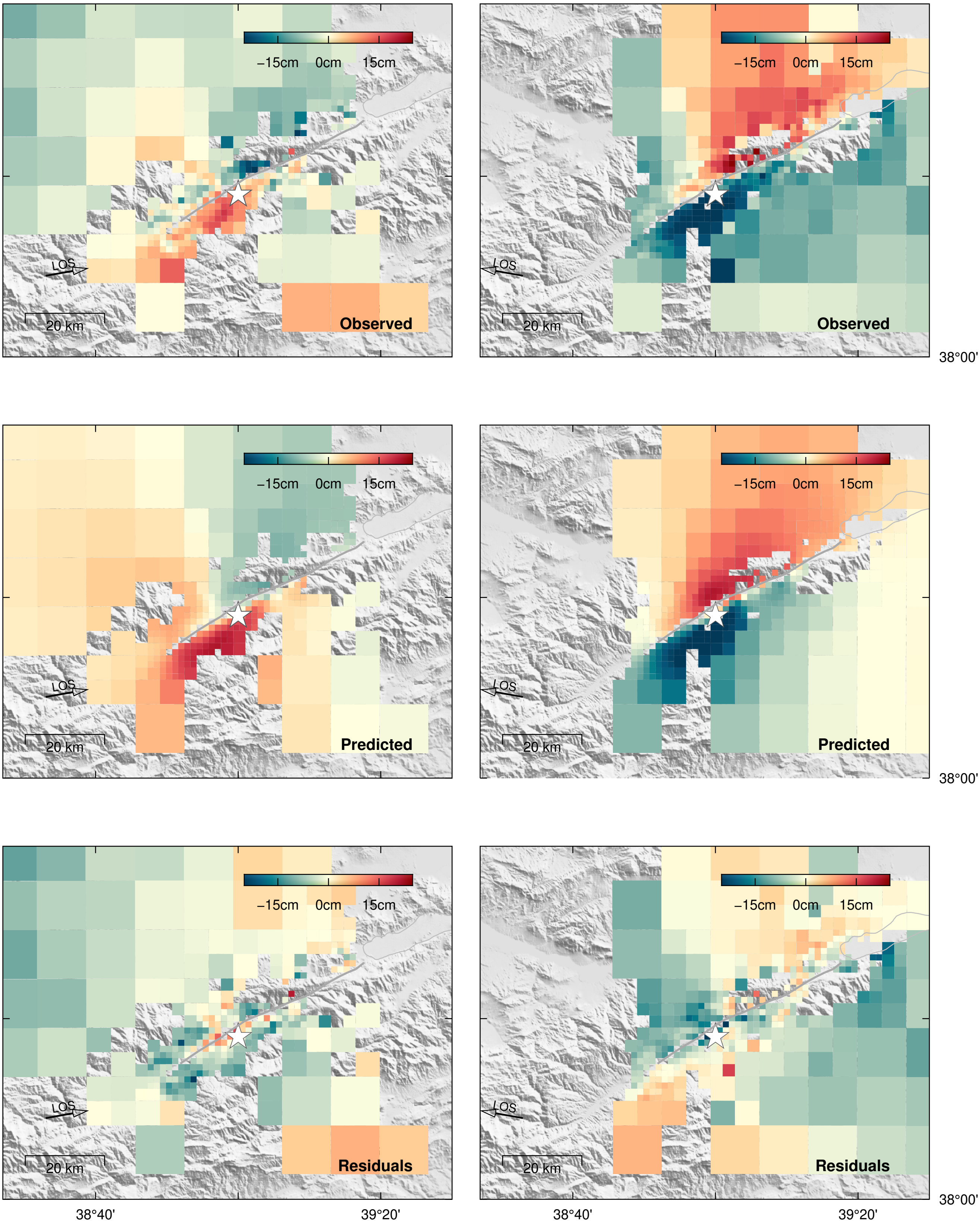

Figure S11. Observed and predicted pixel-offset surface displacement in the satellite azimuth direction for ALOS2 ascending (left) and descending (right) pairs. Predictions are inferred from the average model. The assumed fault trace is shown with a dark gray line.

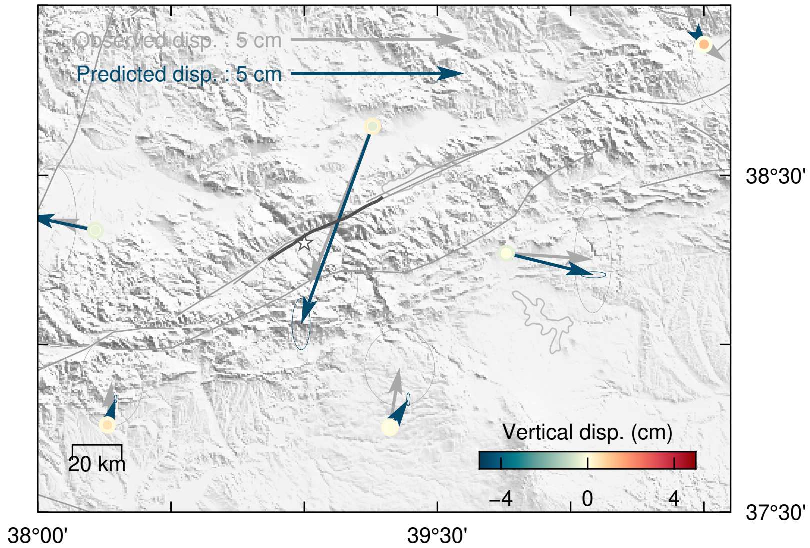

Figure S12. Observed and predicted surface displacement, assuming a planar fault, at the GNSS locations. Observed horizontal surface displacements are shown in gray with 90% confidence ellipses and vertical displacements as the inner amplitudes. Predicted horizontal displacements are shown in blue with 90% confidence ellipses and vertical displacements are the outer amplitudes. The assumed fault trace is shown with a dark gray line and the epicenter is the white star.